UNIVERSITÄT ZU KÖLN

CRC 1601

Leonard Kaiser
I. Physikalisches Institut
Universität zu Köln
kaiser@ph1.uni-koeln.de

The Coherence Length of Galactic Magnetic Fields: Implications for Observations

Leonard Kaiser, Daniel Seifried, Tim-Eric Rathjen, Stefanie Walch

I   Introduction

In this work, we use data from the SILCC simulations [1] to investigate the properties of galactic magnetic fields and how they influence observations, focusing on Faraday rotation.

We show the magnetic field to be coherent over ~50 pc. Additionally, we use synthetic rotation measure observations to investigate how accurately the magnetic field can be determined from observations [2].
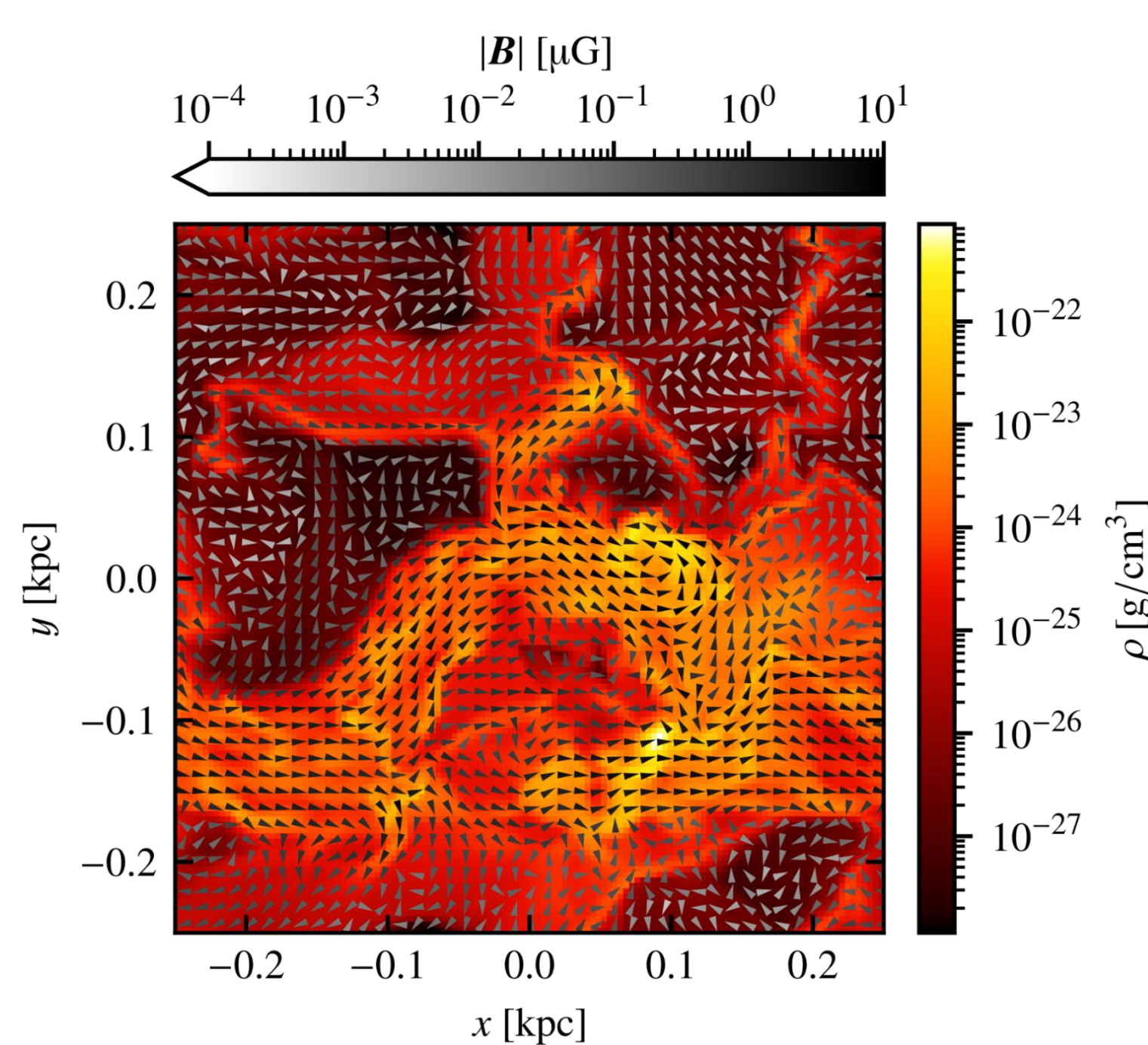

Fig. 1: Slice of the density through a SILCC simulation domain, 100 Myr after the onset of star formation. The magnetic field direction is indicated by arrows showing the magnetic field strength as color. The magnetic field exhibits a complex spatial structure, shaped by stellar feedback.
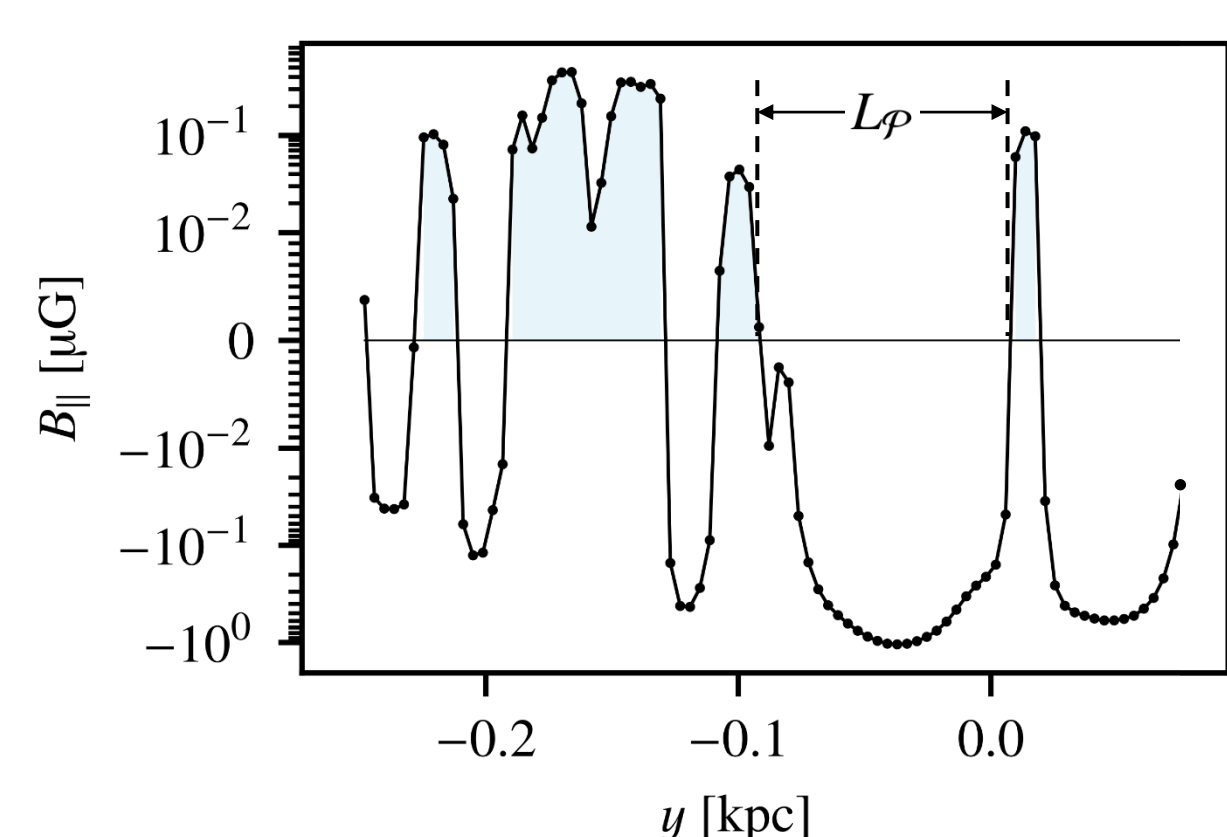
II   Magnetic Field Coherence

Fig. 2: Parallel magnetic field along the y axis. Positive values of $B_\parallel$ are colored in blue. The length of one patch is marked.

Two measures of magnetic field coherence along a line of sight are studied:

- The **patch length** $L_{\mathcal{P}}$ is the length between sign reversals of $B_\parallel$, as shown in Fig. 2.

- The **autocorrelation length** $L_{\mathcal{A}}$ is the integrated autocorrelation function $\mathcal{A}(\Delta l) = (\langle B_\parallel(l)\, B_\parallel(l+\Delta l)\rangle - \mu_{B_\parallel}^2)/\sigma_{B_\parallel}^2$.

The left panel of Fig. 3 shows the distributions of $L_{\mathcal{P}}$ and $L_{\mathcal{A}}$. Both follow a **lognormal** PDF. The time evolution is shown in the right panel. Both measures yield the same **length scale of ~50 pc**, with fluctuations of tens of parsec. This length scale implies a lower limit to the resolution of observational **magnetic field tomography**.
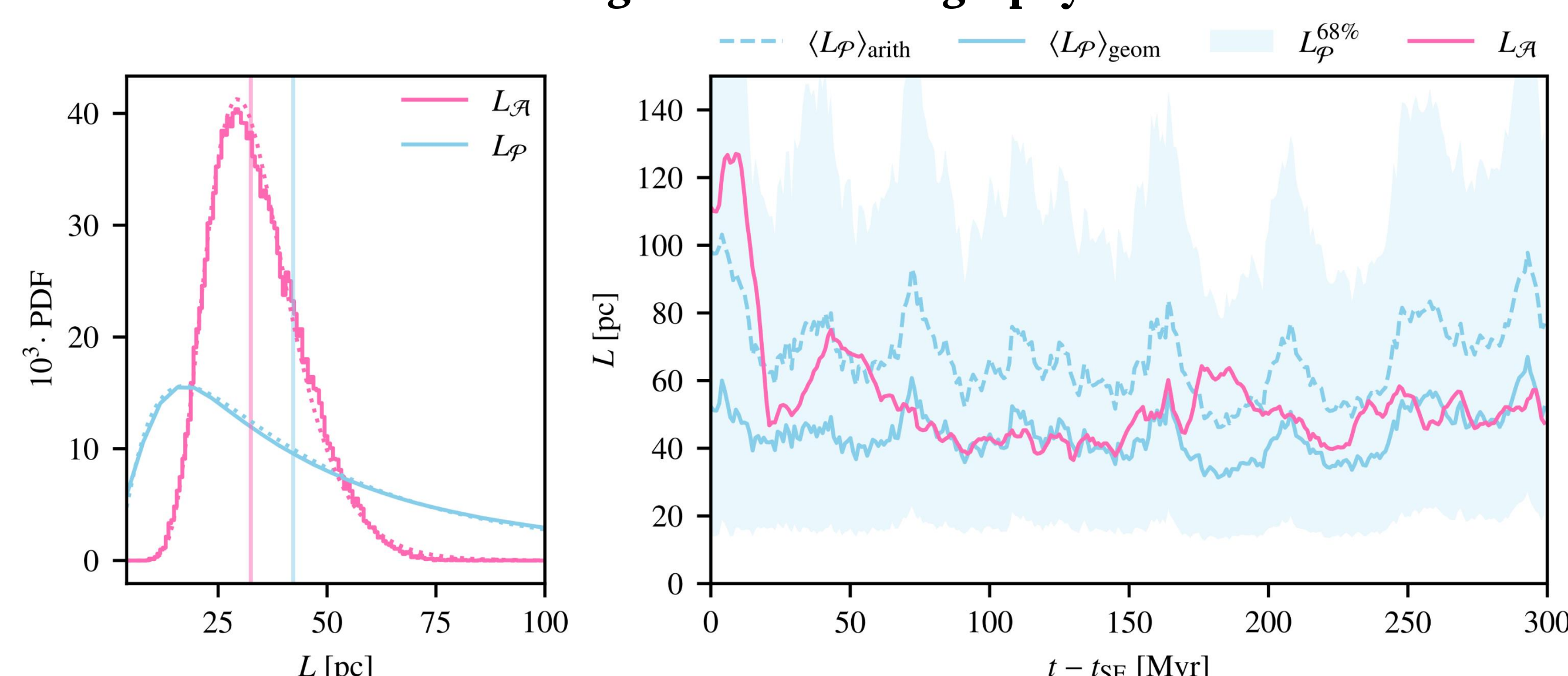

Fig. 3: Left: Distributions of patch and autocorrelation lengths along the y axis, summed for all simulation times $t \gtrsim t_{SF} + 20$ Myr. The distributions are well fitted by lognormal PDFs, shown as dotted lines. The vertical lines indicate the geometric means. **Right:** Autocorrelation length and parameters of the patch length distribution along the y axis against time. Shown are the arithmetic and geometric mean, as well as the 68 % quantile.

V   Conclusion and Outlook

We find the magnetic field to be coherent on scales of ~50 pc, requiring a minimal resolution in observations. The feedback-shaped WIM contributes most strongly to RM. Magnetic field reconstructions from RM are accurate only up to a factor of ~10.

To further study the possibilities and limitations of Faraday rotation observations, we will compute synthetic observations from our simulations using full polarised radiative transfer, including **synchrotron emission** from the cosmic ray population modelled in SILCC.

III   Contribution of B and n_e to RM

Fig. 4: Rotation measure increment dRM_y in a slice of one cell size ($ds \approx 3.9$ pc) thickness at $y = 0$ pc, next to a corresponding slice showing the ISM phases. The colorscale is linear in the interval $[-10^{-5}, 10^{-5}]$ rad/m^2 and logarithmic outside it.
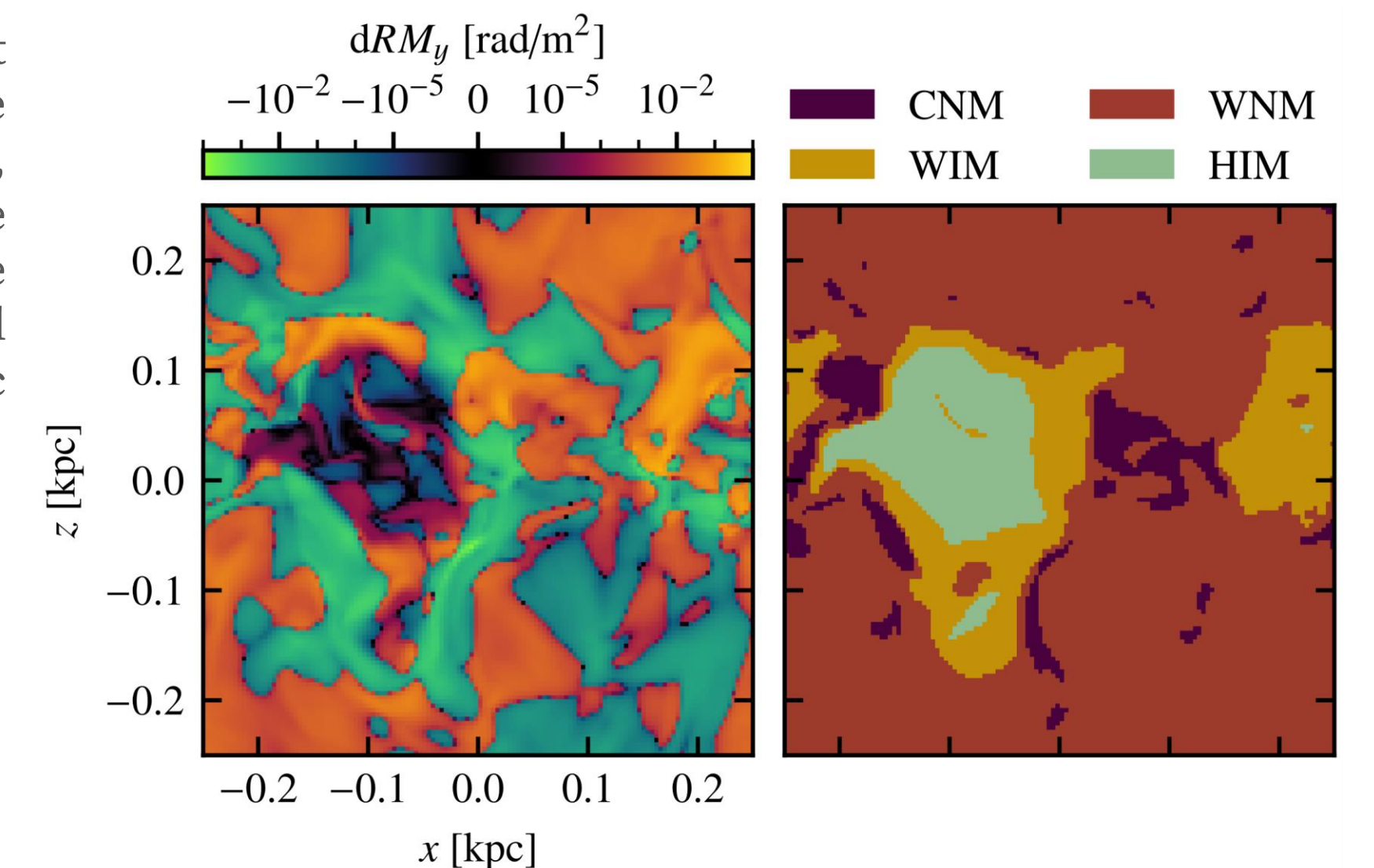
We calculate the rotation measure, $\mathrm{RM} = e^3/(2\pi\, m_e^2\, c^4) \int_l n_e B_\parallel\, \mathrm{d}l$. Fig. 4 shows the RM increment in a layer of cells, compared to the distribution of ISM phases. The highest absolute values are reached in the WIM, and the lowest in the HIM.

In Fig. 5, we show the contribution of the ISM phases to the total RM. The **WIM contributes most strongly** to the RM, closely followed by the WNM. The CNM and HIM contribute least. This is mostly due to the different electron distributions: While the magnetic field reaches similar values in the cold and warm phases, the maximum electron density depends strongly on the ISM phase, as shown in Fig. 6.
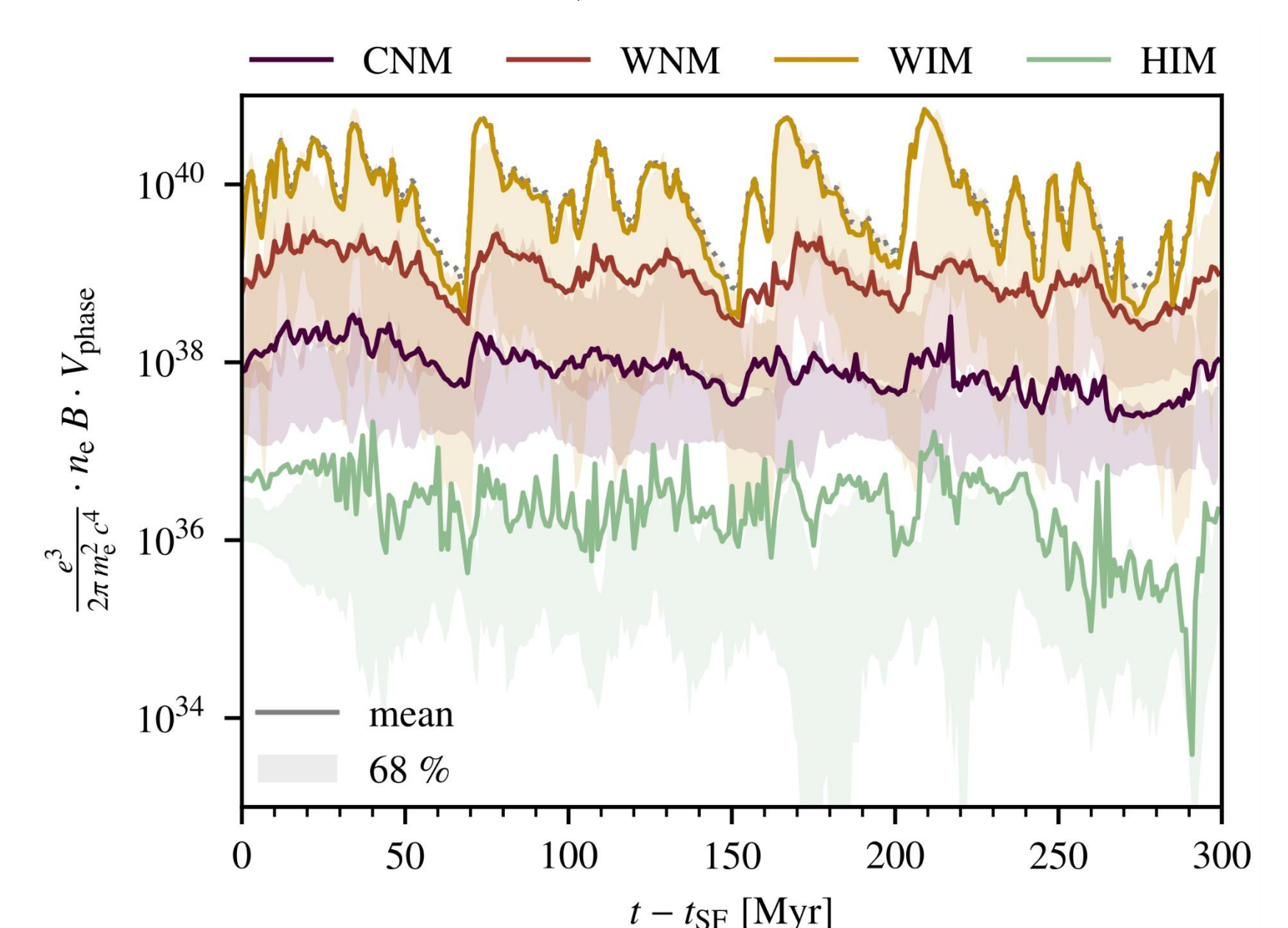

Fig. 5: RM contribution of the ISM phases to the total RM, shown as the dotted line. The lines and the shaded regions show the mean and 68 % quantile, respectively.
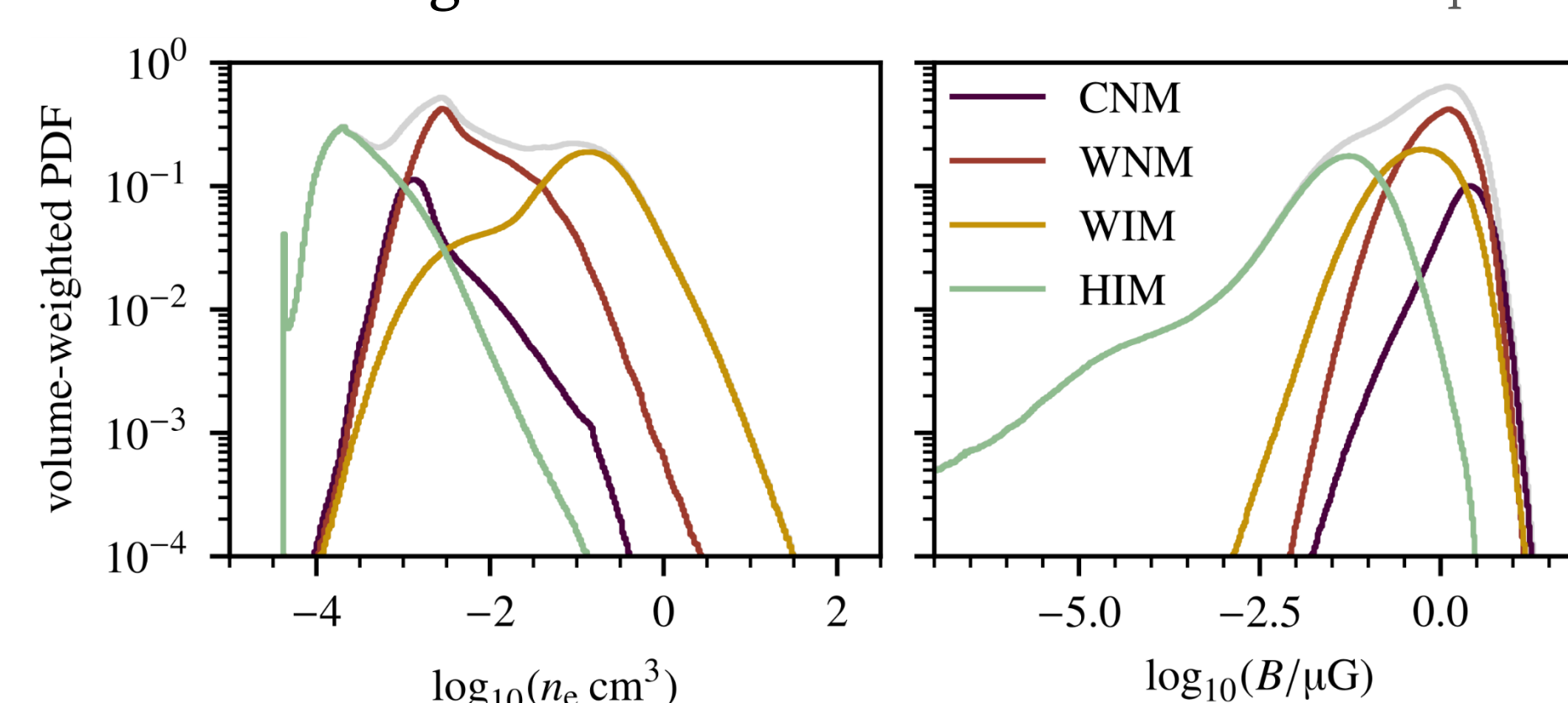

Fig. 6: Left: PDF of the electron number density. All times $t \gtrsim t_{SF} + 20$ Myr are summed. The light grey line represents the total volume. **Right:** Same as left, for the magnetic field strength.

IV   Implications for Observations

For each line of sight, we calculate the actual and reconstructed magnetic field:

- $\langle B_\parallel \rangle = \int_l B_\parallel\, \mathrm{d}l\, /l$
- $B_\parallel^{rec} = \int_l n_e B_\parallel\, \mathrm{d}l\, /(\hat{n}_e l)$
  $\propto \mathrm{RM}/\hat{N}_e$,

assuming a constant electron density $\hat{n}_e = 10^{-2}$ cm^{-3}. The factor $\langle B_\parallel \rangle / B_\parallel^{rec}$ is represented by the diagonal lines in Fig. 7. It **spans about three orders of magnitude** due to large fluctuations in the true electron density. Using a more informed estimate of the electron column density scaled with the hydrogen column density did not significantly reduce the scatter.
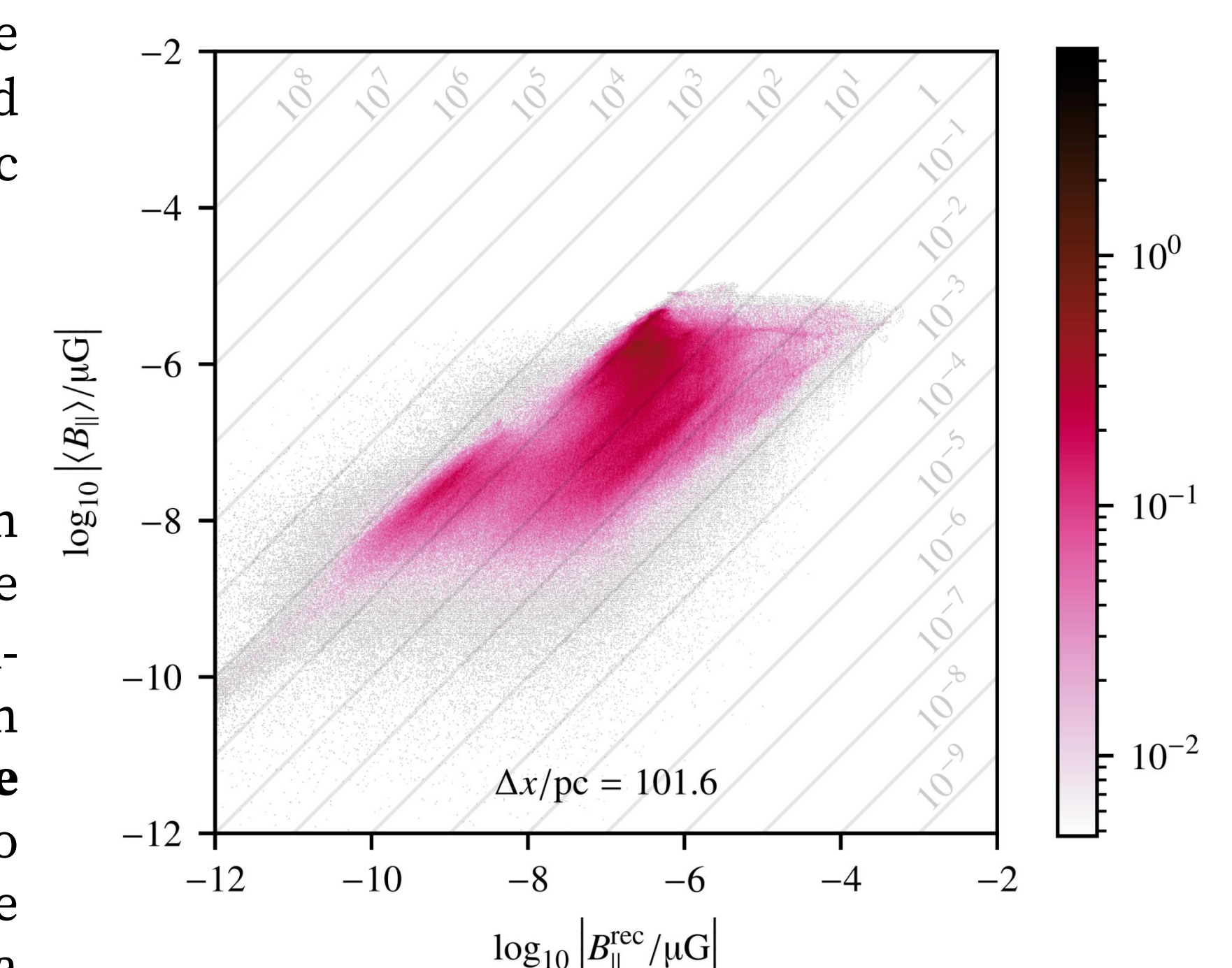

Fig. 7: PDF of the correlation between the average line-of-sight magnetic field $\langle B_\parallel \rangle$ and a reconstruction, $B_\parallel^{rec}$, obtained from the observed RM assuming a constant electron density. The magnetic field can be reconstructed up to a factor of ~10.

References

[1] Rathjen et al. *MNRAS* 522, 1843 (2023) and references therein

[2] Kaiser et al. (in prep.)